JOURNAL OF APPLIED ELECTROCHEMISTRY **19** (1989) 703–712

Gas induced bath circulation in aluminium reduction cells*

A. SOLHEIM, S. T. JOHANSEN, S. ROLSETH, J. THONSTAD

Laboratories of Industrial Electrochemistry and SINTEF, The Foundation for Scientific and Industrial Research at the Norwegian Institute of Technology, N-7034 Trondheim, Norway

Received 26 September 1988; revised 24 January 1989

Gas induced bath circulation in the interpolar gap of aluminium cells was studied in a room temperature physical model and by computer simulation. The circulation velocity increased with increasing gas formation rate, increasing angle of inclination and decreasing bath viscosity, while it was less affected by anode immersion depth, interpolar distance (in the normal range), and convection in the metal. A typical bath velocity near the cathode was 0.05 m s^{-1}. The flow velocity decreased with decreasing bubble size. The results were fitted to a simple semi-empirical expression, and the velocities measured in the model experiments were in good agreement with the findings of the computer simulation.

Nomenclature

A	Surface area (m^2)
c_D	Drag coefficient (1)
c_{pr}	Concentration of 1-propanol (ml/1000 ml)
d_e	Equivalent diameter of gas bubble (m)
F	Faraday constant (96 487 C mol^{-1})
g	Acceleration due to gravity (9.82 m s^{-2})
g_x	Gravity component along anode surface (m s^{-2})
h	Vertical dimension of gas-filled layer (m)
H	Anode immersion depth (m)
i	Current density (A m^{-2})
k	Turbulent energy (m^2 s^{-2})
P	Pressure (N m^{-2})
q	Gas formation rate (m^3 s^{-1} m^{-2})
R	Universal gas constant (8.314 J mol^{-1} K^{-1})
t	Time (s)
U	Liquid velocity parallel to anode surface (m s^{-1})
U_b	Bubble velocity parallel to anode surface (m s^{-1})
U_{rel}	Relative velocity between bubble and liquid (m s^{-1})
V	Liquid velocity perpendicular to anode surface (m s^{-1})
x	Distance from centre of anode (m)
y	Vertical distance from cathode (m)
Y	Interpolar distance (m)
α	Angle of inclination referred to the horizontal (deg.)
ε	Dissipation rate of turbulent energy (m^2 s^{-3})
ϕ	Volume fraction of liquid (1)
ν	Kinematic viscosity μ/ϱ (m^2 s^{-1})
μ	Dynamic viscosity (kg m^{-1} s^{-1})
μ_t	Turbulent viscosity (kg m^{-1} s^{-1})
ϱ	Density of liquid (kg m^{-3})
σ/ϱ	Kinematic surface tension (m^3 s^{-2})
θ	Bubble void fraction (1)

1. Introduction

1.1. *The use of physical models*

Today, transport processes in complicated two-phase flow can be studied by mathematical modelling [1]. The physical relationships involved in the process under study are formulated as partial differential equations which are solved by a digital computer. A significant result from computer simulations is the possibility of coupling the simulated velocity distribution with mass transfer between the boundaries and the bulk flow.

In order to develop and verify theoretical models, physical models play an important role. In many industrial processes the conditions do not allow direct measurements of many parameters, and information which is crucial in order to verify a mathematical model cannot easily be obtained. The Hall–Heroult process for aluminium production is a typical example, due to the lack of flexibility and due to the highly corrosive high temperature system.

The literature on physical modelling of aluminium cells is scarce. Dernedde and Cambridge [2] used a model with water and silicon oil to represent bath and metal, respectively, to study gas induced bath flow in the outer channel and the occurrence of waves at the metal–bath interface. A model containing water was used by Fortin *et al.* [3] who studied the behaviour of gas bubbles underneath the anode. Very large bubbles

---

* Paper presented at the 2nd International Symposium on Electrolytic Bubbles organized jointly by the Electrochemical Technology Group of the Society of Chemical Industry and the Electrochemistry Group of the Royal Society of Chemistry and held at Imperial College, London, 31st May and 1st June 1988.

0021-891X/89 $03.00 + .12

were formed by coalescence. These bubbles had a thick front ($\approx 2\,\mathrm{cm}$ height) and a thinner trailing portion, and they moved with velocities of about $0.3\,\mathrm{m\,s^{-1}}$. Circulation of the bath had little influence on this velocity, but the size of the bubbles increased when gas and liquid moved countercurrently. A 1:10 scale model containing Wood's metal to represent liquid aluminium has been used by Evans *et al.* [4–6] to study the motion induced by magnetic fields. Solheim and Thonstad have used physical models with biphenyl or water to study heat transfer coefficients at the side ledge [7] electrical resistance enhancement due to gas bubbles [8] and mass transfer between the bath and gas bubbles [9].

1.2. *Bath circulation in the interpolar gap*

Bath circulation in aluminium cells is caused by natural convection, gas induced flow, and magnetically induced flow. Theoretical and experimental studies of bath circulation have largely been concentrated on motion set up by magnetic forces. Although such studies have given very valuable insight into flow patterns in metal and bath, the picture is not complete as long as other types of convection are not taken into account.

Gas induced bath motion in the interpolar gap is of particular interest in connection with the transport of alumina and dissolved metal. Gas bubbles travelling underneath the anode exert a force on the surrounding liquid, and in a layer near the anode a flow of bath will be set up moving in the same direction as the gas. The gas bubbles move from the centre of the anode towards the periphery. The flow of liquid out of the interpolar gap along with the bubbles must be replaced by a corresponding oppositely directed flow near the cathode, as sketched in Fig. 1. Nikitin *et al.* [10] measured flow velocities in the interpolar gap of a large Søderberg cell by means of a pitot tube. Near the anode fluid velocities were about $0.35\,\mathrm{m\,s^{-1}}$ in the direction from the anode centre towards the periphery, whereas the corresponding oppositely directed flow near the cathode was calculated to be of the order of $0.04\,\mathrm{m\,s^{-1}}$.

The present paper is focused on the gas bubble induced bath motion, which hitherto has been regarded as less important compared to the magnetically driven flow. The bath flow set up by bubbles which escape from the anode was studied in a physical model, and a simple semi-empirical mathematical model was constructed in order to represent the experimental data. Computer simulations based on fundamental theory were performed for a few experimental conditions, and the results obtained are discussed in relation to the experimental findings.

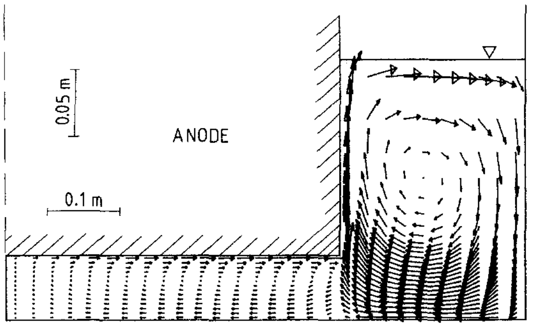

Fig. 1. Flow pattern in the interpolar gap of an aluminium reduction cell.

2. Theory

2.1. *Fundamental treatment*

A mathematical model for the gas induced flow in the interpolar gap must include the interaction of forces between the bath and the gas bubbles as well as the flow in the bulk of the bath. The bath flow is governed by the following conservation equations;
Continuity:

$$\frac{\partial}{\partial x}(\phi\varrho U) + \frac{\partial}{\partial y}(\phi\varrho V) = 0 \tag{1}$$

Momentum conservation:

$$\begin{aligned}\frac{\partial}{\partial x}(\phi\varrho U^2) + \frac{\partial}{\partial y}(\phi\varrho VU) &= -\phi\frac{\partial P}{\partial x} + \frac{\partial}{\partial x}\left[\phi(\mu+\mu_t)\frac{\partial U}{\partial x}\right]\\ &\quad + \frac{\partial}{\partial y}\left[\phi(\mu+\mu_t)\frac{\partial U}{\partial y}\right] + \varrho(1-\phi)g_x\end{aligned} \tag{2}$$

$$\begin{aligned}\frac{\partial}{\partial x}(\phi\varrho UV) + \frac{\partial}{\partial y}(\phi\varrho V^2) &= -\phi\frac{\partial P}{\partial y} + \frac{\partial}{\partial x}\left[\phi(\mu+\mu_t)\frac{\partial V}{\partial x}\right]\\ &\quad + \frac{\partial}{\partial y}\left[\phi(\mu+\mu_t)\frac{\partial V}{\partial y}\right] + \varrho(1-\phi)g_y\end{aligned} \tag{3}$$

In the above equations, U and V are the velocity components parallel and normal to the anode surface, respectively, x and y are the respective coordinates, g_x and g_y are the corresponding components of the acceleration due to gravity (the anode is assumed to be slightly inclined), ϕ is the volume fraction of liquid bath with density ϱ, P is the pressure, μ is the dynamic viscosity, and μ_t is the turbulent viscosity. The latter must be obtained from a turbulence model. The actual turbulence model applied in the computer simulations was the $k-\varepsilon$ model [11].

The volume fraction of gas, or the bubble void fraction (θ), is related to the liquid volume fraction (ϕ) by

$$\theta + \phi = 1 \tag{4}$$

From Equations (2) and (3) for U and V momentum it can be seen that the buoyancy terms, notably $\varrho g(1-\phi) = \varrho g\theta$, increase with increasing gas volume fraction. These terms are responsible for the gas induced motion, and it therefore becomes crucial to model the gas volume fraction accurately. The gas volume fraction must be expressed in terms of the rate of gas evolution at the anode and bubble drift velocities relative to the liquid.

A simple stationary force balance for a bubble, in the direction parallel to the anode surface, can be written

$$\frac{\pi}{4} d_e^2 \varrho \, \tfrac{1}{2} |\boldsymbol{U}_b - \boldsymbol{U}| (U_b - U) c_D = \frac{\pi}{6} d_e^3 (\varrho - \varrho_g) g_x \quad (5)$$

where d_e is the equivalent bubble diameter, i.e. the diameter of a sphere with the same volume as the bubble, U_b and U are the bubble and liquid velocities respectively, c_D is the drag coefficient, and ϱ_g is the density of the gas. From Equation (5) it can be seen that the bubble velocity depends on the fluid velocity, the bubble size, the gravity component along the anode surface, the liquid and gas density (ϱ_g) as well as the drag coefficient c_D. It is noteworthy that the bubble velocity is independent of viscosity (μ), since the drag coefficient is not influenced by μ at high Reynolds numbers. However, in the computations, a more complete force balance given in Ref. [12] was employed.

If we neglect the density of the gas, the relative velocity between the two phases $U_{rel} = U_b - U$ becomes roughly

$$U_{rel} \approx (d_e g_x / c_D)^{1/2} \quad (6)$$

Since the acceleration due to gravity acts nearly normal to the surface of the anode, the gas is located in a two-phase liquid–gas layer near the anode, whereas the major volume of the interpolar space is bubble-free. The volume fraction of gas in the two-phase layer next to the anode is given by

$$\theta = qx / U_b h \quad (7)$$

where q is the rate of gas formation per unit anode surface area ($m^3 \, s^{-1} \, m^{-2}$), x is the distance from the centre of the anode (the bubbles are assumed to move unidirectionally from the centre towards the outer channel), and h is the thickness of the bubble layer. The gas formation rate is calculated from the equation

$$q = \frac{i\mathrm{R}T}{4\mathrm{F}P} \quad (8)$$

where i is the current density, R is the gas constant, T is the absolute temperature, and F is the Faraday constant. By introducing $U_b = U + U_{rel}$ into Equation (7) the buoyancy term in Equation (2) is estimated to be

$$\theta g_x \approx \frac{q x g_x}{h[U + (d_e g_x / c_D)^{1/2}]} \quad (9)$$

Since the buoyancy is driving the liquid flow, it is evident that the liquid velocities will increase with increasing current density (increasing q), increasing anode surface angle of inclination (increasing g_x), and increasing ratio c_D / d_e.

It should be noted that the present treatment with single bubbles cannot be used when there are appreciable concentrations of surface active agents present in the liquid. In that situation, the gas evolution tends to produce several layers of small bubbles close to the anode surface, and the liquid momentum boundary layer will be located outside the bubble region. The physical situation will then be completely different from the assumed behaviour of liquid–bubble interaction.

2.2. *Computational procedures*

A critical step in the applied computational procedure is the modelling of drag forces between the gas bubbles and the liquid. For bubbles sliding underneath the anode, the drag forces acting on the bubbles are expected to be different from the forces acting on free bubbles completely surrounded by liquid. Observations in room temperature physical models [3, 8, 9] indicate that the bubbles will not move like streamlined 'pancakes' underneath the anode. If the bubble surface tension is not too high, the bubbles will easily become unstable and develop a large oscillating projected frontal area normal to the direction of movement. Even so, a bubble moving under a nearly horizontal surface will show a smaller projected frontal area than a bubble of similar volume in free vertical motion. On the other hand, the drag force will be increased, because one part of the bubble is located within the turbulent flow velocity layer. Hence, there are arguments in support of comparing the drag force for a bubble sliding along the anode boundary layer to the drag force for a free bubble.

Due to the lack of information concerning drag forces for bubbles moving under a nearly horizontal surface, the drag law for free bubbles was employed. Hence, for Reynolds numbers, $\mathrm{Re} = \varrho(U_b - U)d_e/\mu$, considerably higher than unity, the drag coefficient (c_D) only depends on the Eötvös number (Eo) and the volume fraction of gas [12];

$$c_D = \frac{0.622(1 - \theta^{2/3})\,\mathrm{Eo}}{1 + 0.235\,\mathrm{Eo}}, \quad \mathrm{Eo} = g d_e^2 (\varrho - \varrho_g)^2 \varrho \sigma \quad (10)$$

where σ is the surface tension.

The numerical technique for solving the momentum equations was based on the finite difference approach and the SIMPLE algorithm for pressure given by Patankar [15]. The solution of the coupled equations started with a computation of bubble trajectories underneath the anode for a quiescent bath. The bubbles were released at 20 equispatial points underneath the anode surface. A Lagrangian transport equation, which originates from a force balance for single bubbles, was solved numerically for a set of bubbles. The bubble void fraction was related to the residence time of the bubble in each control volume of the studied domain. The bubble fraction (θ) was then calculated from the bubble velocity and the rate of formation of gas, and the results was inserted into the momentum equations. The momentum, pressure, and turbulence equations were then solved iteratively. However, after a few iterations, the bubble trajectories and the bubble void fractions were recalculated for the new bath flow field. By switching between calculations of void fraction from bubble trajectories and iterations on the liquid transport equations it was possible to obtain a converged solution. The boundary condition for the bubbles was the reflection at solid walls (anode). When a bubble reached the surface of the bath, the trajectory calculation was aborted. For the liquid bath, standard wall functions were applied in order to relate the near-wall velocity to the wall shear stress [14]. Similar wall functions were used for the turbulent energy (k) and its dissipation rate (ε) [14]. The applied technique had earlier produced very reliable results for bubble driven flows in metallurgical ladles [12, 13]. More details about the computational procedure are found in Ref. [12].

2.3. *Simplified treatment*

In many situations it will be convenient to have an equation where the liquid velocities in the interpolar gap can be expressed explicitly. In the following, an attempt is made to derive such an equation.

We start by assuming that the velocity of the bubbles can be expressed as

$$U_b = f[q, x, g, \mu, \varrho, \sigma, \sin\alpha] \tag{11}$$

where α is the angle of inclination of the anode surface to the horizontal. The velocity also depends on the bubble size (d_e). However, d_e is assumed to be a function of the parameters listed in Equation (11). Three basic units (kg, m, s) and eight variables give five dimensionless groups, e.g.

$$\underset{\text{I}}{\frac{U_b^3}{qxg}} = f\left[\underset{\text{II}}{\left(\frac{qx}{\nu}\right)}, \underset{\text{III}}{\left(\frac{\varrho g x^2}{\sigma}\right)}, \underset{\text{IV}}{\left(\frac{\varrho^3 g \nu^4}{\sigma^3}\right)}, \underset{\text{V}}{\sin\alpha}\right] \tag{12}$$

where we have introduced the kinematic viscosity $\nu = \mu/\varrho$. It can be seen that the groups II and III have the same form as the Reynolds and Eötvös numbers, respectively, whereas group IV is the Morton number (M).

In previous work [8], the accumulated volume of gas underneath the anode was measured in a physical model. The value of θh, which equals the gas volume per unit anode surface area, could be expressed as

$$\theta h \sim q^{0.6} x^{0.6} (\sin\alpha)^{-0.4} \tag{13}$$

By combining Equations (7) and (13) we obtain

$$U_b \sim (qx \sin\alpha)^{0.4} \tag{14}$$

which is introduced in Equation (12) to yield

$$U_b \sim (qx\sin\alpha)^{0.4} \frac{g^{0.33}}{\nu^{0.07}} f[\text{M}] \tag{15}$$

where M is the Morton number. As a very rough approximation, we assume proportionality between U_b and the liquid velocity, U. In addition, U will evidently be a function of the dimensionless distance from the liquid metal y/Y where Y is the interpolar distance. However, this function can only be determined experimentally or by computer analysis. With the given assumptions, the velocity of the liquid in the interpolar space roughly varies as

$$U \sim (qx \sin\alpha)^{0.4} \left(\frac{g^{0.33}}{\nu^{0.07}}\right) f[\text{M}, y/Y] \tag{16}$$

The time needed for a liquid element to move between two points x_1 and x_2 at the same level y/Y is found by integrating Equation (16),

$$t \sim \left[0.6(q \sin\alpha)^{0.4} \left(\frac{g^{0.33}}{\nu^{0.07}}\right) f(\text{M}, y/Y)\right]^{-1} (x_1^{0.6} - x_2^{0.6}) \tag{17}$$

2.4. *Requirements for model liquids*

From the fundamental equations the so-called model laws may be derived. They require that the model and the real system (the prototype) should be (i) geometrically similar, i.e. have the same shape, and (ii) dynamically similar, i.e. have equal relationships between forces. The first requirement also comprises the gas bubbles. A model shaped as a vertical section of the prototype will be satisfactory if forces or velocities in one of the horizontal directions can be neglected. In a full scale model, the requirement of dynamic similarity will be fulfilled when the kinematic viscosity and the kinematic surface tension of the bath σ/ϱ are kept equal in model and prototype. This can be achieved by the use of water. A suitable liquid representing the molten metal should possess the following properties,

1) Proper density, $\approx 1100\,\text{kg}\,\text{m}^{-3}$
2) Proper kinematic viscosity, $\approx 0.2 \times 10^{-6}\,\text{m}^2\,\text{s}^{-1}$ (very low)
3) Proper interfacial tension, $\approx 0.25\,\text{N}\,\text{m}^{-1}$ (very high)
4) Low mutual solubility and high chemical stability.

Such a liquid does not exist. However, if the conditions at or near the anode are to be studied, it can be assumed that the absence of 'metal' does not affect the fluid dynamics in that area. Thus use of a separate 'metal' phase will then be unnecessary. In other cases it may be satisfactory to select a 'metal' phase that gives a proper density ratio between 'metal' and 'bath'.

3. Experimental

3.1. *The model cell*

The most important features of the model cell are highlighted in Table 1. The model cell was constructed as a full scale vertical section of a Søderberg aluminium cell, and it consisted of a Plexiglas container partly filled with 'bath' (water) into which the box-shaped 'anode' was immersed (see Fig. 2). The 'anode', which fitted tightly between the walls of the container, was divided into three compartments. No separate 'metal' phase was used. The 'interpolar distance', i.e. the distance between the 'anode' and the bottom of the container, could be adjusted by means of the threaded rods indicated in the figure. Anodic

Table 1. Comparison between physical model and industrial cell

	Model	*Ind. Cell*
Bath	Water	Fluoride melt
Metal	No 'metal'	Aluminium
Bath temperature, °C	7	960
Kinematic viscosity of bath, $m^2 s^{-1}$	1.5×10^{-6}*	$\approx 1.5 \times 10^{-6}$
Kinematic surface tension, $m^3 s^{-2}$	7.3×10^{-5}*	$\approx 6.3 \times 10^{-5}$
Anode material	Porous bronze	Carbon
Gas evolution	Compressed air	Electrolytic (CO_2)
Gas bubble size	Variable**	Not known

* Can be varied by additives, e.g. glycerol and 1-propanol, or by changes in temperature
** By the addition of 1-propanol

gas evolution was simulated by passing compressed air through the bottom of the 'anode', which consisted of porous bronze plates (Pacific Sintered Metals Co., USA). The gas flow was controlled by means of three rotameters; one for each 'anode' compartment. The cell was supported on an aluminium frame which permitted the entire cell to be tilted in the longitudinal direction.

When the anode was strictly horizontal one huge flattened gas bubble was formed which eventually covered the entire surface area. Therefore it was necessary to operate with a certain angle of inclination in order to obtain a steady regular gas flow. This situation may not be quite representative for industrial cells, even though the anode in practice will attain a certain curvature and angle of inclination due to variations in the metal level caused by magnetic forces. When the 'anode' was given a certain angle of inclination, the picture was dominated by huge flattened bubbles with a thick front (1–2 cm) and a thinner trailing part, as described by Fortin *et al.* [3]. These bubbles were often as wide as the 'anode' and several centimetres long. Such slugs of gas engulfed all smaller bubbles on their way along the 'anode' surface. A completely different situation arose when 1-propanol was added to the water. The bubbles then became relatively small (1–5 mm) and they moved as a froth-like continuous blanket.

3.2. *Measurements*

The average liquid velocity was determined by adding coloured liquid in the outer channel, i.e. the volume outside the interpolar gap, and the movement of the colour front was recorded by means of lasers. Two laser heads were located at one side of the cell, and the intensity of the the light was registered by means of photodetectors which were located at the opposite side of the cell and connected to a recorder. The time (t) needed for the colour to move from the location of the first beam at a distance x_1 from the 'centre' of the anode to the second beam at a distance x_2 was read from the graph. The laser beams were always placed at a level corresponding to $y/Y = 0.4$, e.g. 2 cm above the bottom of the cell when the 'interpolar distance' was $Y = 5$ cm. However, due to some turbulent dispersion, the measured time corresponded to the maximum velocity rather than the velocity at that particular level. A typical recording is shown in Fig. 3. Because some time was needed to set up the circulating motion, the first measurement was performed at least five minutes after starting the gas flow.

4. Results

The majority of the measurements in the physical model were performed with a fixed interpolar distance

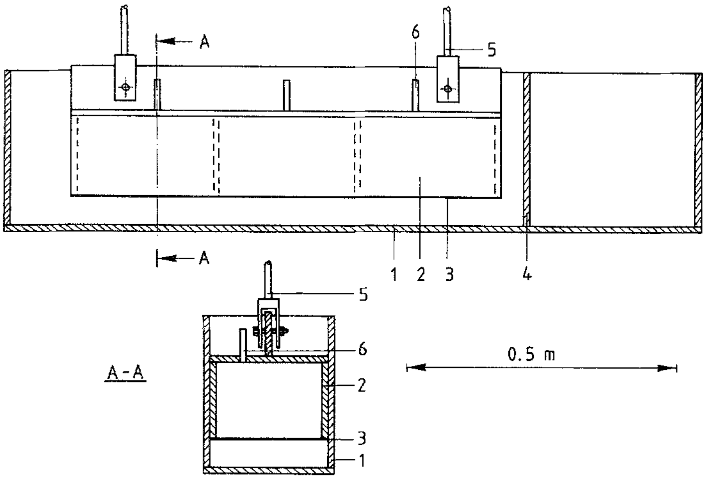

Fig. 2. Sketch of the model cell. 1, container; 2, 'anode'; 3, porous bronze plates; 4, removable partition wall; 5, threaded rod; 6, air inlet.

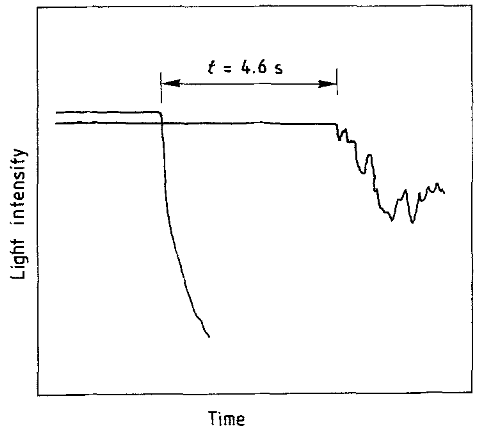

Fig. 3. Light intensity recorded by the photodetectors as a function of time.

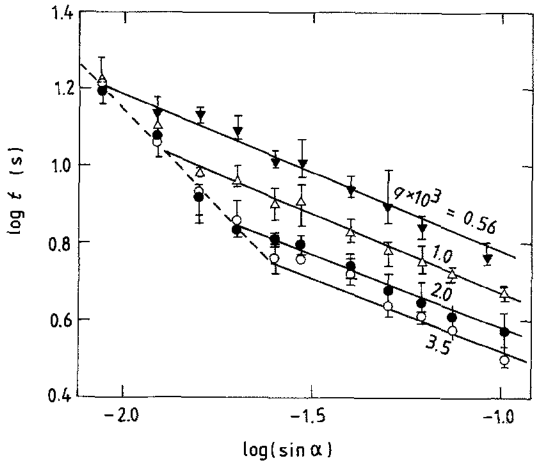

Fig. 5. Experimental residence time as a function of the angle of inclination at different gas formation rates as indicated in the figure.

of 5 cm. The anode immersion depth (measured at the edge of the anode) was zero, in order to reduce any interference with the circulating bath motion in the outer channel. No surface active agents were added to the 'bath'. The time between the extinction of the laser beams in different positions by the added colour was measured in four series of experiments with the following variables; gas evolution rate (q), angle of inclination (α), laser beam positions (x_1, x_2), and kinematic viscosity (ν). The results are plotted in Figs 4–7 where the points represent average values of typically three measurements and the bars represent the highest and the lowest values.

According to Equation (17) plots of log (t) versus log (q) should produce straight lines with slopes of -0.4. The slopes of the solid lines in Fig. 4 are very close to this value. However, at low angles of inclination the time becomes independent of the rate of gas evolution. A similar trend is observed in Fig. 5, where plots of log (t) versus log (sinα) give slopes in accordance with Equation (17), provided that the angle of inclination is not too small. From Figs 4 and 5 we find that the velocity depends only upon the angle of inclination when the rate of gas evolution is high and the angle of inclination is small. It was observed that the combination of small angles and high gas evolution rates produced very large bubbles which spread out and gave a high fraction of the surface area covered with gas.

The effect of viscosity is shown in Fig. 6. The viscosity was varied by changing the temperature of the 'bath' rather than the composition, in order to avoid any unwanted effects of additives, e.g. variations in the bubble size. In Equation (17), the function of the Morton number (M) must be $M^{-0.03}$ in order to produce the experimentally observed slope. The magnitude of M will normally be between 10^{-11} and 10^{-10} for water as well as for industrial baths.

The effect of varying the laser beam positions is demonstrated in Fig. 7. A straight line through the origin was produced when the time was plotted versus ($x_1^{0.6} - x_2^{0.6}$), in accordance with Equation (17).

Considering the seemingly dubious assumptions made in the derivation of Equation (17) the fit is remarkably good, as shown in Fig. 8. The straight line in Fig. 8 represents the equation

$$t = 5.06\left[(q \sin \alpha)^{0.4}\left(\frac{g^{0.33}}{\nu^{0.07}}\right) M^{-0.03}\right]^{-1} (x_1^{0.6} - x_2^{0.6}) \tag{18}$$

Correspondingly, the velocity in the bath at the level

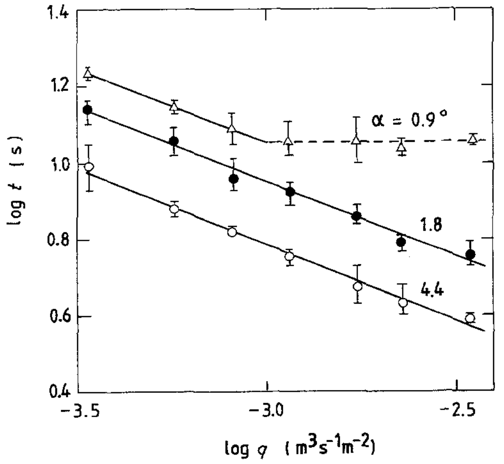

Fig. 4. Experimental residence time as a function of gas formation rate at different angles of inclination of the anode as indicated in the figure.

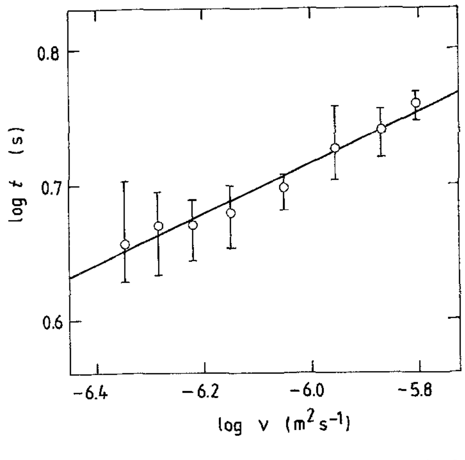

Fig. 6. Experimental residence time as a function of the kinematic viscosity of the bath.

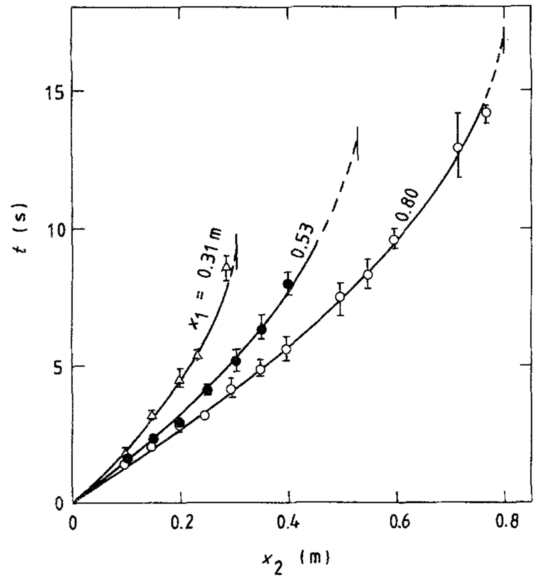

Fig. 7. Experimental residence time as a function of the positions of the laser beam.

y/Y = 0.4 becomes

$$U = 0.329(qx \sin \alpha)^{0.4}\left(\frac{g^{0.33}}{\nu^{0.07}}\right)M^{-0.03} \quad (19)$$

The correlation between experimental residence time and residence time as calculated by the computer shows good agreement, as demonstrated in Fig. 9. The experimental residence times are generally somewhat lower than the theoretical ones, which may be due to turbulent dispersion of the added colour.

Velocity vectors calculated by the computer are shown in the subsequent figures. The input data were: $q = 2 \times 10^{-3}\,\mathrm{m^3\,s^{-2}}$ (corresponding to a current density of $7570\,\mathrm{A\,m^{-2}}$), $\alpha = 2°$, and $\nu = 1 \times 10^{-6}\,\mathrm{m^2\,s^{-1}}$. The maximum velocity from right to left, i.e. towards the centre of the anode, is found to be about $0.05\,\mathrm{m\,s^{-1}}$, in agreement with Equation (19) which gives $U = 0.058\,\mathrm{m\,s^{-1}}$ at $x = 0.4$ m away from the centre of the anode.

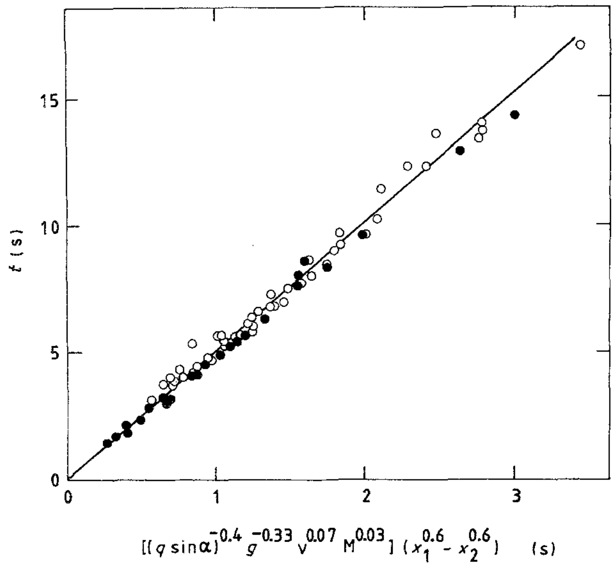

Fig. 8. Experimental residence time plotted according to Equation (17). Open circles – data from Figs 4 and 5, filled circles – data from Fig. 7.

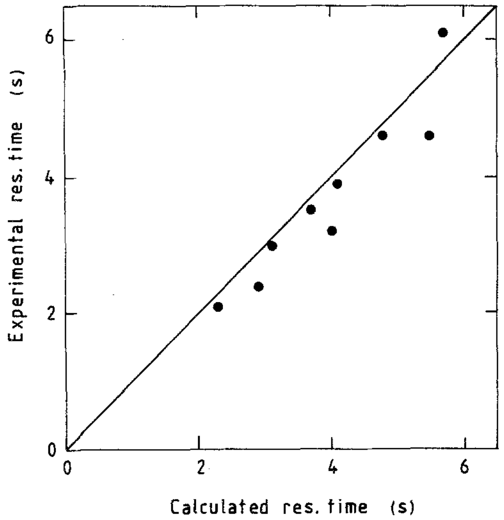

Fig. 9. Comparison between experimental residence time and residence time as calculated by the computer for different combinations of angle of inclination (α = 1–3°) and gas formation rate ($q = 1\text{–}3 \times 10^{-3}\,\mathrm{m^3\,s^{-1}\,m^{-2}}$).

4.1. *Anode immersion depth*

The effect of anode immersion depth (H) is shown in Fig. 10. The width of the outer channel, i.e. the distance between the edge of the anode and the partition wall shown in Fig. 2, was 17.5 cm and the interpolar distance was 5 cm. The influence of the anode immersion depth was very slight, which indicates that bath motion in the interpolar gap and in the outer channel may be treated as two independent phenomena. This was confirmed by the computer simulations. As can be seen from Fig. 11, variation in the anode immersion only affects the flow pattern in the vicinity of the anode edge.

4.2. *Interpolar distance*

The influence of the interpolar distance (Y) is shown in Fig. 12 (model experiments) and in Figs 11a and 13 (computer simulations). For interpolar distances above 3 cm, the velocity was nearly independent of the interpolar distance. A slight increase in the vertical

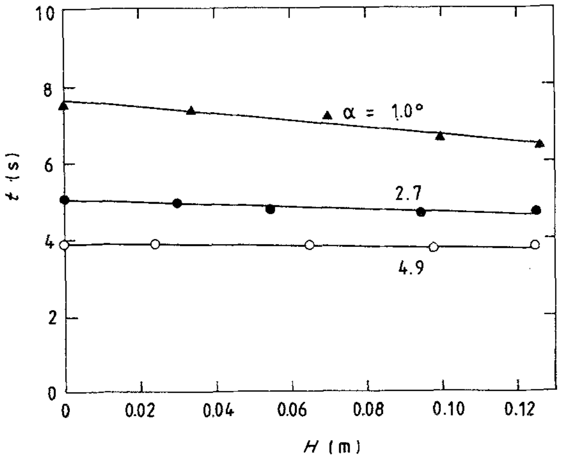

Fig. 10. Experimental residence time as a function of the anode immersion depth at three different angles of inclination as indicated in the figure.

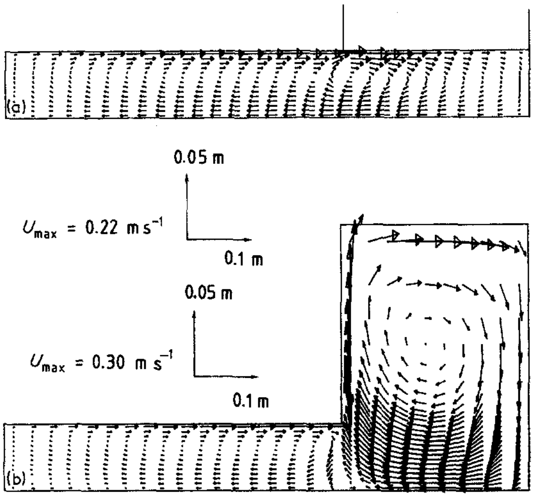

Fig. 11. Velocity vectors calculated by the computer at 0 (a) and 0.15 m (b) anode immersion depths.

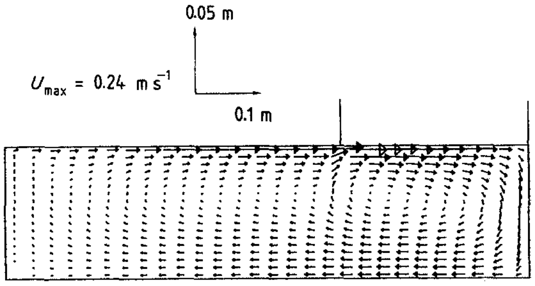

Fig. 13. Velocity vectors at interpolar distance 0.10 m as calculated by the computer.

dimensions of the gas bubbles was observed with decreasing interpolar distance, as mentioned in an earlier work [8]. A maximum in the bubble height was found at $Y \approx 3$ cm (see below). The decreasing velocity when the interpolar distance was reduced below this value can be associated with the fact that the bubbles reduced their height and spread out on the 'anode' surface, approaching the 'slug' flow regime. This will probably not take place in practice, since the cathode consists of liquid metal.

4.3. *Bubble size*

The bubble size was lowered substantially by the addition of 1-propanol. Measured times between the extinction of each laser beam are plotted versus concentration of 1-propanol in Fig. 14. The times increased for additions up to 0.5 volume per cent, whereas additions exceeding this value had no further effect, even though the surface tension continued to decrease. Similar trends were observed earlier [8], when it was found that addition of 1-propanol up to a certain amount brought about an increase in the volume of accumulated gas, the maximum increase corresponding to a factor of 2.4. This is in fair agreement with the data in Fig. 14, from which a reduction in velocity by a factor of about two can be seen. According to the Gibbs adsorption isotherm, the surface of the gas bubbles becomes saturated with 1-propanol approximately at the point where no further changes with increasing concentration could be detected. This suggests that the observed phenomena are caused by the reduced tendency to coalescence due to repulsive forces between the bubbles, rather than being an effect of decreased surface tension in itself.

4.4. *Effect of liquid metal phase*

In the computer simulations the bottom of the cell was assumed to be solid, as in the physical model. It is difficult to perform a proper simulation with two liquid phases present, due to the formation of interfacial waves which would have a substantial effect on the drag coefficient between the phases. However, the flow pattern in the bath could be computed with a moving bath–metal interface, as shown in Fig. 15. The figure shows that it makes little difference if the bottom is moving towards the left or towards the right with a velocity of 0.1 m s^{-1}. The velocity of the inter-

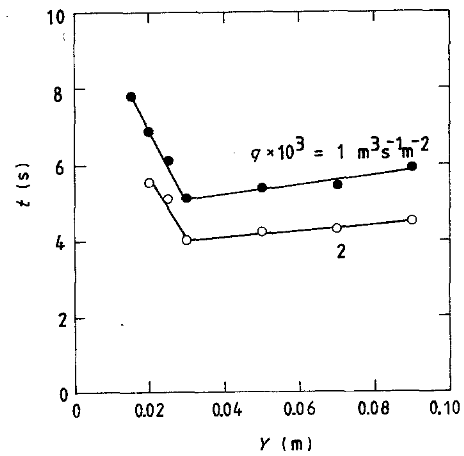

Fig. 12. Experimental residence time as a function of the interpolar distance at two different gas formation rates as indicated on the figure.

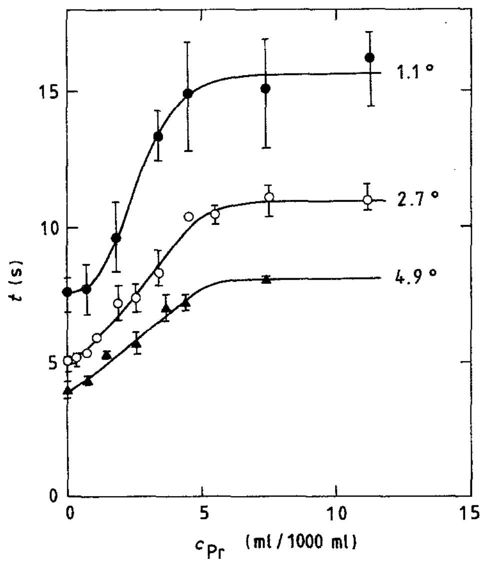

Fig. 14. Experimental residence time as a function of the concentration of 1-propanol at different angles of inclination as indicated on the figure.

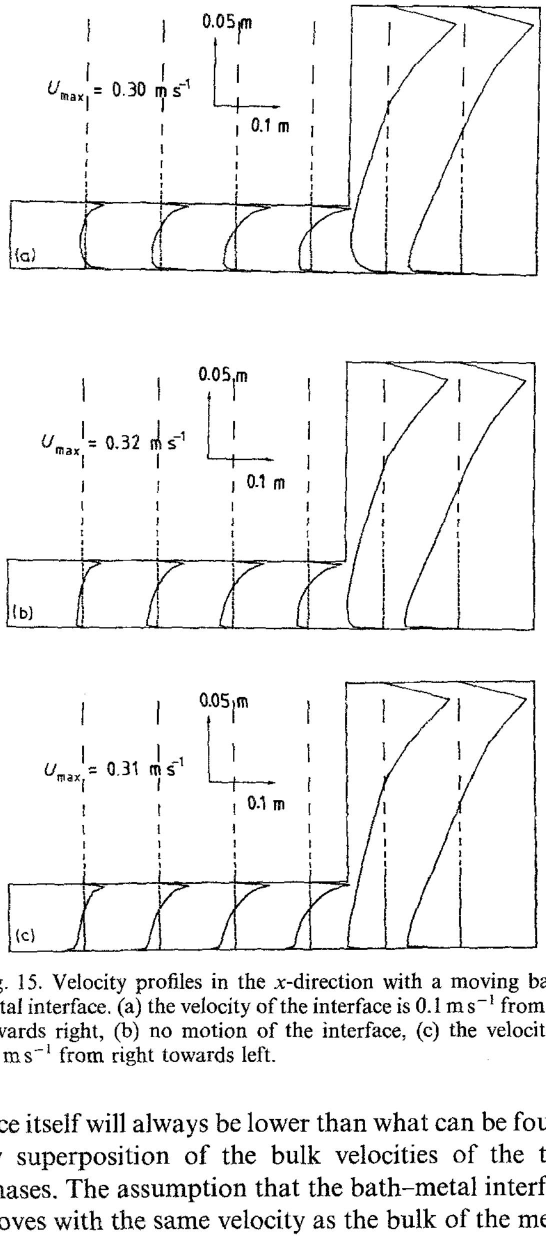

Fig. 15. Velocity profiles in the x-direction with a moving bath–metal interface. (a) the velocity of the interface is 0.1 m s^{-1} from left towards right, (b) no motion of the interface, (c) the velocity is 0.1 m s^{-1} from right towards left.

face itself will always be lower than what can be found by superposition of the bulk velocities of the two phases. The assumption that the bath–metal interface moves with the same velocity as the bulk of the metal would therefore in this context lead to an overestimation of the influence of metal flow velocity, and it can be stated that the error in the model experiments caused by the absence of a separate 'metal' phase is not significant.

5. Discussion

Arthur [16] analysed samples taken from the interpolar gap of an industrial aluminium cell, and found a vertical concentration gradient with respect to dissolved metal across the interpolar gap. It has been suggested that the transport of dissolved metal, and hence the current efficiency, is partly governed by turbulent diffusion through the bulk of the bath [17]. However, according to the results of the present work it is rather improbable that convection in the bulk of the bath represents any significant resistance against transport of dissolved metal. Due to the circulating pattern of the gas induced flow, all the bath entering the interpolar gap will be transported up into the vicinity of the gas bubbles where the contents of dissolved metals, at least partly, will be oxidized. The average vertical velocity in the direction from the cathode towards the anode can be estimated to be of the order of 10^{-3} m s^{-1}, which should be compared to the overall mass transfer coefficient for dissolved metal ($\approx 10^{-5}$ m s^{-1}). Additionally, dissolved metal is transported across the interpolar gap by turbulent dispersion. For these reasons, the main component of the overall mass transfer coefficient and hence the rate determining step(s) for the metal reoxidation must be sought elsewhere. It is reasonable to assume that the rate of reoxidation is limited by mass transfer at the bath–metal interface.

The gas induced circulation velocity in the interpolar gap is relatively high, at least of the same magnitude as the magnetically induced convection. It therefore seems proper to take gas induced convection into consideration in mathematical models concerning bath flow. There was very good agreement between the computer simulation and the measured velocities, so that in principle, the proper bath velocities may be estimated in a computer simulation which takes all kinds of flow into consideration. The current efficiency largely depends on the relative velocities of bath and metal, and the gas induced convection becomes increasingly more important the more successful the magnetic field compensation becomes.

The relatively thick bubble fronts observed in the model cell experiments are believed to be realistic. Typically, the bubbles extend vertically 1–2 cm from the surface of the anode, and obviously such bubbles may cause disturbances in the bath–metal interface especially at small interpolar distances. It has been suggested [18] that the sharp drop in current efficiency below a certain critical interpolar distance is caused by metal waves touching the anode. However, it seems more appropriate to explain this phenomenon by direct contact between gas bubbles and metal waves. The lower limit for the interpolar distance then corresponds to the sum of bubble height and wave amplitude. More information about wave amplitudes is needed, and such work is in progress. We believe that a more fundamental understanding of the behaviour and the effect of gas bubbles is of great importance in order to optimize the performance of aluminium reduction cells.

The volume between the anode and the side ledge appears to be critical for the current efficiency, as both gas induced and magnetically induced bath velocities are high in that area. The results obtained by computer simulations underline the need of keeping a proper side ledge which extends towards the projection of the anode, in order to reduce the metal surface area in that part of the cell.

Acknowledgements

Financial support from the Royal Norwegian Council for Scientific and Industrial Research and from the Norwegian aluminium industry is gratefully acknowledged. Some of the experiments in the physical model were performed by Mr E. Skybakmoen.

References

[1] W. Rodi, '*Turbulence Models and Their Application in Hydraulics – a State of the Art Review*', IAHR-Publication (1980).

[2] E. Dernedde and E. L. Cambridge, *Light Metals 1975, Vol. 1*, pp. 111–112 (Proceedings, 104th AIME Annual Meeting 1975).

[3] S. Fortin, M. Gerhardt and A. J. Gesing, *Light Metals 1984*, pp. 721–741 (Proceedings, 113th AIME Annual Meeting, Los Angeles, 1984).

[4] H.-C. Lee and J. W. Evans, *Light Metals 1985*, pp. 569–579 (Proceedings, 114th AIME Annual Meeting, New York, 1985).

[5] J. W. Evans and S. K. Banerjee, *Light Metals 1986*, pp. 535–539 (Proceedings, 115th AIME Annual Meeting, New Orleans, 1986).

[6] S. K. Banerjee and J. W. Evans, *Light Metals 1987*, pp. 247–255 (Proceedings, 116th AIME Annual Meeting, Denver, 1987).

[7] A. Solheim and J. Thonstad, *J. Metals* **36** (3) (1984) 51.

[8] A. Solheim and J. Thonstad, *Light Metals 1986*, pp. 307–403 (Proceedings, 115th AIME Annual Meeting, New Orleans, 1986).

[9] A. Solheim and J. Thonstad, *Light Metals 1987*, pp. 239–245 (Proceedings, 116th AIME Annual Meeting, Denver, Colorado, 1987).

[10] A. V. Nikitin, V. A. Kryukovskii and N. S. Mikhalitsin, *Tsvetn. Met./Non-Ferrous Metals* **16** (8) (1975) 37.

[11] B. E. Launder and D. B. Spalding, 'Mathematical Models of Turbulence', Academic Press, London (1982).

[12] S. T. Johansen and F. Boysan, *Met. Trans. B.*, **19** (1988) 755.

[13] F. Boysan and S. T. Johansen, 'Mathematical Modelling of Gas-Stirred Reactors', International Seminar on Refining and Alloying of Liquid Aluminium and Ferro-Alloys, Trondheim, Norway, 1985, Aluminium-Verlag GmbH, Düsseldorf, pp. 267–288.

[14] B. E. Launder and D. B. Spalding, *Comp. Meths. Appl. Eng.* **3** (1974).

[15] S. V. Patankar, 'Numerical Heat Transfer and Fluid Flow', Hemisphere, New York (1982).

[16] A. M. Arthur, *Met. Trans.* **5** (1974) 1225.

[17] R. F. Robl, W. E. Haupin and D. Sharma, *Light Metals 1977, Vol. 1*, pp. 185–202 (Proceedings, 106th AIME Annual Meeting, 1977).

[18] R. Bacchiega and A. Lama, *TRAVAUX ICSOBA* **11** (16) (1981) 227.